

AstroSat observation of the HBL 1ES 1959+650 during its October 2017 flaring

Zahir Shah^{1*}, Savithri H. Ezhikode^{1†}, Ranjeev Misra¹ and Rajalakshmi T. R.²

¹Inter-University Center for Astronomy and Astrophysics, Post Bag 4, Ganeshkhind, Pune, India - 411007

²School of Pure & Applied Physics, Mahatma Gandhi University, Kottayam, Kerala, India - 686560

Accepted XXX. Received YYY; in original form ZZZ

ABSTRACT

We present the results of the X-ray flaring activity of 1ES 1959+650 during October 25-26, 2017 using *AstroSat* observations. The source was variable in the X-ray. We investigated the evolution of the X-ray spectral properties of the source by dividing the total observation period (~ 130 ksecs) into time segments of 5 ksecs, and fitting the SXT and LAXPC spectra for each segment. Synchrotron emission of a broken power-law particle density model provided a better fit than the log-parabola one. The X-ray flux and the normalised particle density at an energy less than the break one, were found to anti-correlate with the index before the break. However, a stronger correlation between the density and index was obtained when a delay of ~ 60 ksec was introduced. The amplitude of the normalised particle density variation $|\Delta n_\gamma/n_\gamma| \sim 0.1$ was found to be less than that of the index $\Delta\Gamma \sim 0.5$. We model the amplitudes and the time delay in a scenario where the particle acceleration time-scale varies on a time-scale comparable to itself. In this framework, the rest frame acceleration time-scale is estimated to be $\sim 1.97 \times 10^5$ secs and the emission region size to be $\sim 6.73 \times 10^{15}$ cms.

Key words: galaxies: active – BL Lacertae objects: general – BL Lacertae objects: individual: 1ES 1959+650 – galaxies: jets – X-rays: galaxies

1 INTRODUCTION

Blazars are radio-loud Active Galactic Nuclei (AGN) with powerful relativistic jet pointing close to the line of sight of observer (Urry & Padovani 1995). The small inclination of relativistic jet results in Doppler boosted emission and other extreme properties from blazars like rapid variability across the electromagnetic spectrum (Böttcher et al. 2003) and non-thermal emission extending from radio to GeV/TeV energies (Ulrich et al. 1997). The spectral energy distribution (SED) of blazars has two prominent broad components: low energy component which peaks at optical/UV/X-ray energies and high energy component which peaks at MeV/GeV energies. According to leptonic model, two different emission processes are responsible for this broadband emission viz. the synchrotron process in which highly relativistic leptons in the presence of magnetic field produces radio to UV/X-ray energies (Bregman et al. 1981) and the inverse-Compton (IC) process in which low energy seed photons gets up-scattered to high energies giving rise to X-ray/GeV/TeV spectrum. The seed photons for the IC scattering can be

synchrotron photons produced by the same population of leptons (synchrotron self Compton (SSC): Jones et al. 1974, Maraschi et al. 1992, Ghisellini et al. 1993) or photons entering external to jet (external Compton (EC): Dermer et al. 1992, Sikora et al. 1994, Błażejowski et al. 2000, Shah et al. 2017). On the other hand, the high energy emission in blazars can be also produced by relativistic protons via hadronic processes, such as the proton synchrotron process and pion production (Mannheim & Biermann 1992; Mücke & Protheroe 2001). Based on the characteristics of their optical spectrum, blazars are broadly classified as BL Lac objects and Flat Spectrum Radio Quasars (FSRQ). They are also classified based on the peak frequency of the synchrotron component: Low energy peaked BL Lac objects (LBLs; $\nu_{p,syn} < 10^{14}$ Hz), Intermediate energy peaked BL Lac objects (IBLs; $10^{14} \text{ Hz} < \nu_{p,syn} < 10^{15}$ Hz) and High energy peaked BL Lac objects (HBLs; $\nu_{p,syn} > 10^{15}$ Hz) (Abdo et al. 2010). In case of HBL sources, single population of relativistic electrons generally produces the broadband emission in such a way that radio to X-ray emission is attributed to synchrotron process while hard X-ray to γ -ray emission is attributed to SSC process (Mastichiadis & Kirk 1997). HBLs are generally less variable in optical band than LBL sources

* E-mail: zahir@iucaa.in

† savithri@iucaa.in

(Gaur 2014; Hovatta et al. 2014), however during the flaring their variability increases by significant amount.

1ES 1959+650 is an HBL source located at redshift $z=0.048$ (Perlman et al. 1996). This source was first observed in radio band using NRAO Green Bank Telescope (Gregory & Condon 1991), and later the X-ray emission from it was detected during the Einstein IPC Slew Survey (Elvis et al. 1992). The VHE emission from 1ES 1959+650 was first detected by the Seven Telescope Array group in 1999 (Nishiyama 1999) and it became among the first extragalactic sources detected at VHE energies (Holder et al. 2003). Numerous exceptional flaring events has been reported from 1ES 1959+650 across the electromagnetic spectrum (EMS) including the intense activity at very high energies (GeV/TeV). In addition to broad emission like features, 1ES 1959+650 also exhibits orphan TeV flares (Krawczynski et al. 2004; Aliu et al. 2014). During the simultaneous multi-wavelength flaring, the X-ray and γ -ray fluxes of 1ES 1959+650 are well correlated, which is usually explained in-terms of one-zone Synchrotron Self-Compton (SSC) models. However, orphan VHE flare challenges such interpretation and instead models like hadronic synchrotron mirror model are incorporated to explain such flares (Böttcher 2005). Further, the uncorrelated multi-wavelength emission can be also explained by multi-zone SSC or (Graff et al. 2008) or EC process (Krawczynski et al. 2004).

The X-ray spectrum of 1ES 1959+650 varies significantly during the active states. In this source, the correlation between the X-ray flux and the spectral shapes have been studied in several works (e.g. Giebels et al. 2002; Gutierrez et al. 2006; Kapanadze et al. 2016a, 2018b; Patel et al. 2018; MAGIC Collaboration et al. 2020). These correlation study showed that the spectral hardening increases as the flux increases i.e., *harder-when brighter* behaviour is observed, a general feature found in blazar (e.g. Ulrich et al. 1997; Gliozzi et al. 2006; Hayashida et al. 2015; Kapanadze et al. 2017). Gutierrez et al. (2006) showed that *harder-when brighter* behaviour in flares on time scales of days is caused by a variation of the Doppler factor, the magnetic field, and/or break energy, whereas the shift of the maximum energy of accelerated electrons drives the longer timescales (months time scale) correlation between flux and spectral index. The *harder when brighter* behaviour on longer timescales is additionally accompanied by higher variability amplitude at harder energies and vice versa (Gliozzi et al. 2006). This behaviour is also associated with the shift in the synchrotron peak of the SED (Kapanadze et al. 2016a, 2018a). The synchrotron peak shift towards higher energy as the flux increases and vice versa. Further, *harder when brighter* spectrum together with the hysteresis loop in the hardness ratio–flux plane provides important information about the acceleration and cooling process: the clockwise pattern indicates that the acceleration timescales are smaller than the cooling timescale, whereas anticlockwise pattern is expected when acceleration and cooling timescales are same (Kirk & Mastichiadis 1999; Kapanadze et al. 2018a).

Several enhanced flux states has been reported from 1ES 1959+650 over broadband energy, during the period 2015–2016 (e.g., Kapanadze et al. (2016b)). During this period, 1ES 1959+650 had shown prolonged X-ray activity with powerful X-ray emission, it reached in a state of record

count rate ($> 20 \text{ counts s}^{-1}$) in the energy range of 0.3–10 KeV (Kapanadze et al. 2016b). This outburst placed 1ES 1959+650 to the list of only three blazars detected with X-ray count rate exceeding 20 counts s^{-1} . Another X-ray flaring activity was observed in the source (Kapanadze 2017) since 2017 June. The Neil Gehrels Swift Observatory (here after *Swift*) X-ray telescope (XRT) observations reported a count rate (0.3–10 keV) of $\sim 39 \text{ counts s}^{-1}$ in September 2017, much higher than the value reported in the previous year (Kapanadze et al. 2018a). A month later, a Target of Opportunity observation of the source was triggered with *AstroSat*. The observation showed a 0.7–30 keV flux of $\sim 1.4 \times 10^{-9} \text{ erg cm}^{-2} \text{ s}^{-1}$ similar to the simultaneous *Swift* observation taken on 2017 October 25.

In this work, we report the X-ray and UV analysis of *AstroSat* observations of 1ES 1959+650 during October 2017. The high flux rate and rapid variability in the X-ray band allowed for time-resolved spectral analysis which revealed correlated spectral parameter variations on time-scales of hours. We interpret the results by comparing with predictions obtained from solving the linearized kinetic equation for particle distribution having sinusoidal perturbations. In the next section, we provide details of the data acquisition and reduction, while in section §3 we report the temporal and spectral analysis of the observed data. In section §4, we present the time-dependent model and compare its predictions with the results. In section §5 the results are summarised and discussed.

2 DATA REDUCTION

1ES 1959+650 was observed by *AstroSat* during 25-26 October, 2017 for a total duration of ~ 135 ks. *AstroSat* (Agrawal 2017), being a multi-wavelength observatory equipped with Ultra-Violet Imaging Telescope (UVIT; Tandon et al. (2017a,b)), Soft X-ray focusing Telescope (SXT; Singh et al. (2017, 2016)), Large Area X-ray Proportional Counter (LAXPC; Yadav et al. (2016b)) and Cadmium Zinc Telluride Imager (CZTI; Rao et al. (2017)), allows the simultaneous monitoring of the source at UV, soft X-ray and hard X-ray bands. For this study we use the simultaneous observations of the source with LAXPC, SXT and UVIT. The observed and/or processed data for the observations were obtained from the *AstroSat* data archive ASTROBROWSE. All the instrument specific software and tools for processing the data, and other important links are available in the ASSC website¹.

SXT is an X-ray imaging telescope that operates in the 0.3–8 keV energy band (Singh et al. 2017, 2016). The source 1ES 1959+650 was observed in the Photon Counting (PC) mode with SXT. We processed the Level-1 data of the source through the SXT pipeline version 1.4a (ASISXTLevel2-1.4a release date: December 06, 2017), using the calibration database (CALDB). The cleaned Level-2 event files for different orbits were merged with the SXTEVTMERGER tool. We then used the merged event file to create the science products using XSELECT version V2.4d. SXT spectra and light

¹ http://astrosat-ssc.iucaa.in/?q=data_and_analysis

Table 1. Details of the LAXPC, SXT and UVIT observations of 1ES 1959+650 during October 2017 flaring.

Instrument	Energy band	Exposure ksec	Count rate counts s ⁻¹
LAXPC10	3-30 keV	60	60.80±0.21
LAXPC20	3-30 keV	60	58.23±0.72
SXT	0.7-7 keV	30	13.98±0.02
UVIT	FUV-BaF2 (1541 Å)	14	4.37±0.03
	NUV-N2 (2792 Å)	14	2.55±0.03

curves were extracted for a circular region of the source with 16 arcmin radius.

LAXPC consists of three units of identical X-ray proportional counters (LAXPC10, LAXPC20 & LAXPC30) and can perform observation in a broad range of 3 keV to 80 keV (Antia et al. 2017; Misra et al. 2017; Yadav et al. 2016a; Agrawal et al. 2017). LAXPC30 has been switched off due to gain instability issues (Antia et al. 2017), hence data from the other two LAXPC units were used for the analysis. The processing of Level-1 data and further analysis were done with the software LAXPCSOFT. Since the source is faint above ~30 keV in LAXPC we utilised the scheme of faint source background implemented as a part of LAXPCSOFT for extracting the background spectra and light curves for LAXPC 10 & LAXPC 20.

The source was observed simultaneously with UVIT. For UVIT analysis, we obtained the Level-2 data for the observation directly from ASTROBROWSE. The Level-1 data were already processed with the pipeline UVIT LEVEL-2 PIPELINE (UL2P) version 6.3 (CALDB version - 20190625) by the payload operation team. The observation was made in PC mode in both FUV and NUV bands with BaF2 & N2 filters, respectively.

The details of the UV and X-ray observations of the source are given in Table 1. Further analysis carried out for the study are given in the following sections.

3 ANALYSIS

3.1 Time-Variability

We generated the light curves from the SXT, LAXPC and UVIT observations of 1ES 1959+650 to check the time-variability of the source. Figure 1 shows the UV and X-ray light curves of 1ES 1959+650.

A total of 11 orbit data were available for both FUV and NUV bands. We obtained the count rates from the combined Level-2 images of each orbit. The source count rates were extracted from circular regions of 30 pixels (~ 12.5'') radius such that it includes ~ 97% of the source flux (Tandon et al. 2017b). Background counts were extracted from multiple source free circles of 60-pixel radii, away from the source. The background subtracted FUV and NUV light curves plotted in Fig 1 show that the source is marginally variable in both NUV and FUV bands. In order to confirm if the source is variable we checked the light curves of two stars in the field. The non-variability of the stars show that the source is intrinsically variable.

The SXT light curves were generated for different time bins in the 0.7–7 keV band. The quantum efficiency of SXT is poor at low energy (Singh et al. 2017), hence we ignored the SXT spectra below 0.7 keV. We used XSELECT for creating the light curves, the middle panel in the left side of Fig 1 shows the same for a bin size of 100 sec, while upper panel in the right side of Fig 1 corresponds to 5 ksec binned SXT light curve. The variability of the light curves was checked with the FTOOL LCSTATS and we found that the source is variable with a fractional rms variability, F_{rms} obtained in the 100 sec and 5 ksec binned light curves as 0.085 ± 0.004 and 0.084 ± 0.012 , respectively. The LAXPC (10 & 20) light curves were also extracted for a bin size of 100 sec and 5 ksec. In the LAXPC, the spectra above 30 keV was ignored due to strong background. The lower panels of Fig 1 show these light curves in the 3–30 keV energy band. We also calculated the F_{rms} of the source in LAXPC using LCSATS. The F_{rms} in the 100 sec and 5 ksec binned LAXPC 10 light curves are obtained as 0.171 ± 0.004 and 0.166 ± 0.023 , respectively. While in the 100 sec and 5 ksec binned light curves of LAXPC 20, the F_{rms} values are obtained as 0.158 ± 0.004 and 0.154 ± 0.023 , respectively. These results indicate that the source is variable in the LAXPC observations as well.

3.2 X-ray spectral analysis

We analysed the X-ray spectra of the source using XSPEC version 12.9.0n. The X-ray spectra were analysed in the energy band of ~ 0.7–30 keV, where the SXT spectral data were included from 0.7 keV to ~7 keV and LAXPC data were ignored below 4 keV and above ~ 30 keV. The background spectrum for SXT was produced from blank-sky observations by SXT POC. For LAXPC, the background spectra were generated using the code for the faint source background provided by LAXPC team. We have used `sxt_pc_mat_g0to12.rmf` as SXT response matrix file (RMF). The ancillary response file (ARF) for the SXT instrument was obtained using the standard PC mode ARF and the `sxt_ARFModule` Version: 0.02 released in 2019 July.

Throughout the fitting procedure we applied a systematic error of 3%. While fitting the SXT spectrum we need to incorporate the energy shift in the response matrix. For this we used `gain fit` command with the slope frozen at 1, and the offset was obtained around 0.03 keV. The SXT spectrum was grouped such that each bin has minimum 1000 counts and LAXPC spectra were grouped at 5% level to obtain three energy bins per resolution. The time-averaged spectra of SXT, LAXPC 10 and LAXPC 20 were fitted simultaneously with three different models, power-law, log-parabola and broken power-law, corrected for the Galactic absorption using the XSPEC routine `TBabs`. A constant was multiplied to the SXT spectra to take into account any systematic variation in the effective areas of the SXT and LAXPC units. These models were convolved with the synchrotron emissivity function (Rybicki & Lightman 2008) using an XSPEC local convolution model `Synconv` written by us. Once convolved with `Synconv` these models represent particle distribution of the emitting region instead of photon distribution. Specifically the “Energy” variable in the convolved XSPEC model should be interpreted as being $\xi = \sqrt{C}\gamma$, where γ is the Lorentz factor of the particle and $C = 1.36 \times 10^{-11} \delta B / (1 + z)$ with δ being the Doppler

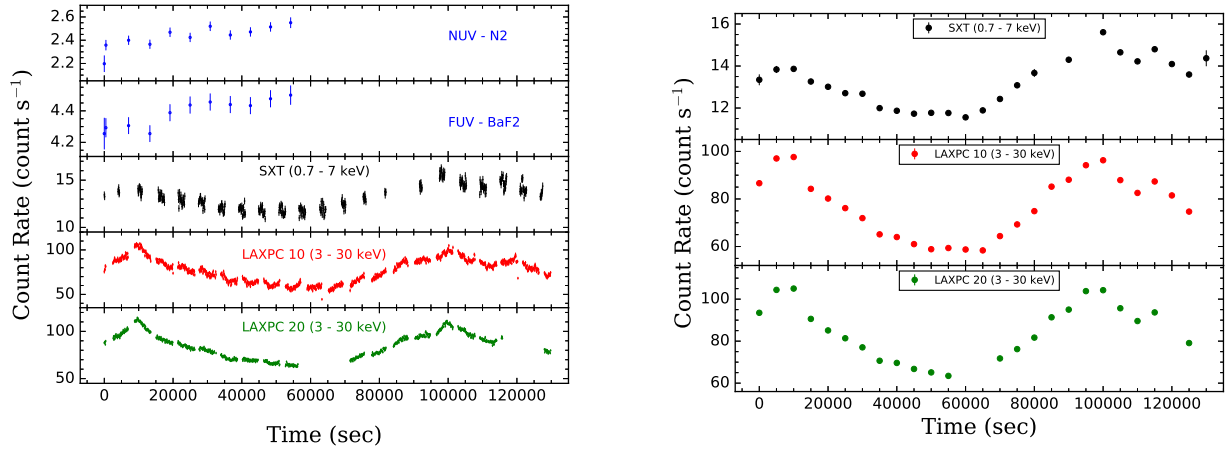


Figure 1. X-ray and UV light curves of 1ES1927+654 *AstroSat* observations taken in October 2017. Left side: upper two panels show UVIT NUV-N2 and FUV-BaF2 observations, the middle panel shows the simultaneous 100 sec binned SXT light curve in the 0.7–7 keV band and the hard X-ray 100 sec binned light curves (3–30 keV) from LAXPC10 & LAXPC20 observations are plotted in the lower panels. Right side: upper panel corresponds to the 5 msec binned SXT light curve in the 0.7–7 keV band, middle and lower panel corresponds to the 5 msec binned LAXPC10 & LAXPC20 light curves (3–30 keV), respectively.

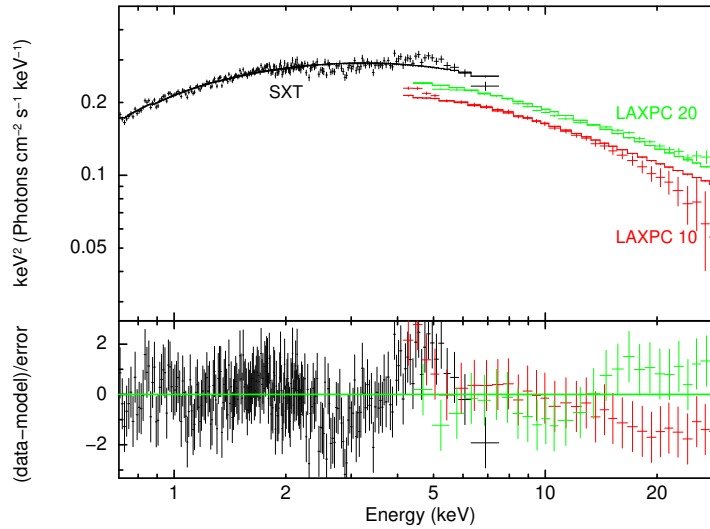


Figure 2. The time-averaged SXT and LAXPC spectra (0.7–30 keV) of 1ES1959+650 fitted with the model $constant \times TBabs(Synconv \otimes bknpower)$. Upper panel: Unfolded spectra plotted with the model. Lower panel: Residuals for the spectral fit.

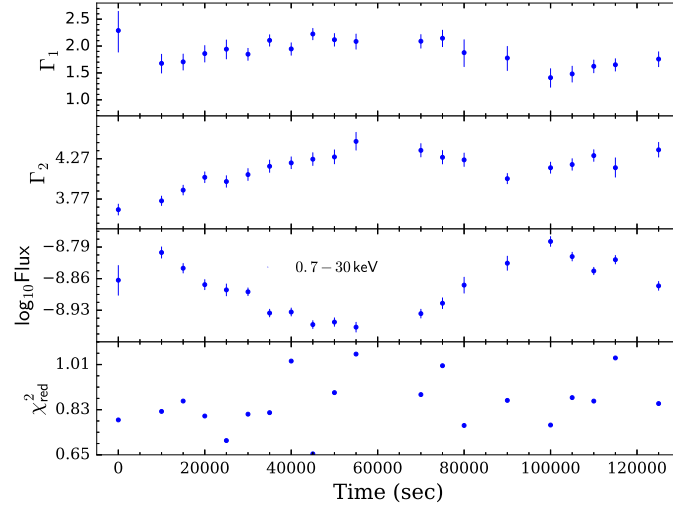


Figure 3. Best-fit results from the time-resolved spectral analysis using the model $\text{constant} \times \text{TBabs}(\text{Synconv} \otimes \text{bknpower})$. The first three panels show the variability of the particle indices (Γ_1 & Γ_2) and the logarithm of flux ($\text{erg cm}^{-2} \text{s}^{-1}$) in the 0.7–30 keV band. The reduced χ^2 value obtained for the spectral fit in each time-resolved segment is given in the lower panel.

factor, z the red-shift and B the magnetic field strength. Thus, any parameter of the model, such as the break energy in the broken power-law model ξ_{brk} , would be related to γ as $\gamma_{brk} = \xi_{brk} / \sqrt{C}$ and one can relate a corresponding break in the photon energy spectrum $E_{brk} = C\gamma_{brk}^2 = \xi_{brk}^2$. The spectral fits with the synchrotron convolved power-law, log-parabola and broken power-law models resulted in $\chi^2(\text{dof})$ values of 1320.04/(279), 309.36/(278) and 286.73/(277) respectively. The best-fit parameters of these models fitted for the time-averaged spectra are given in Table 2. Due to the very large χ^2 we discarded *power-law* in the later analysis. The broken power-law provides a better fit compared to the other models and the spectral fit and residual for the model $\text{constant} \times \text{TBabs}(\text{Synconv} \otimes \text{bknpower})$ is shown in Fig. 2. The flux obtained for this model in the 0.7–30 keV range is $\sim 1.4 \times 10^{-9} \text{erg cm}^{-2} \text{s}^{-1}$. The spectral fit obtained by freezing the hydrogen column density, N_H to the value given in LAB survey (Kalberla et al. 2005) resulted in higher χ^2 values than those acquired when N_H was kept free. Therefore, in order to obtain better fit statistics, the N_H was set as a free parameter. The obtained values of N_H are lower than those obtained from LAB survey group.

Since the source is highly variable in the soft and hard X-ray bands we investigated the time evolution of X-ray spectral properties of the source during observation. Here,

we employed the method of time-resolved spectroscopy, where the total observation period was divided into time segments of 5ksec. For each of the time segment we created SXT and LAXPC spectra. In this analysis, we used only SXT and LAXPC 20 spectra because LAXPC 20 background is more stable than LAXPC 10.

Since the broken power-law yielded a better fit statistic than the log-parabola one for the time averaged spectrum, we use it for the time resolved analysis. However, the break energy E_{brk} (or ξ_{brk}^2), was not well constrained and hence we fix its value to 2.86 keV obtained during the time-averaged spectral fitting. The ξ_{brk} and N_H parameters were fixed at the values obtained for the time-average spectral fit where the relative error in normalisation is minimum. We note that since the model is being convolved with synchrotron emissivity function, the indices of the broken power-law model represent the indices of the particle distributions i.e. Γ_1 and Γ_2 are the indices of power law distributions before and after the break energy.

The best-fit parameters for the time-resolved spectral analysis are plotted in Figure. 3 and are also given in Table 3. A strong anti-correlation (Spearman's method; rank ~ -0.8 , p-value $\sim 2.5 \times 10^{-5}$) is observed between the flux and Γ_1 (see Fig. 4), which is the hardening when brightening behaviour previously reported in blazars.

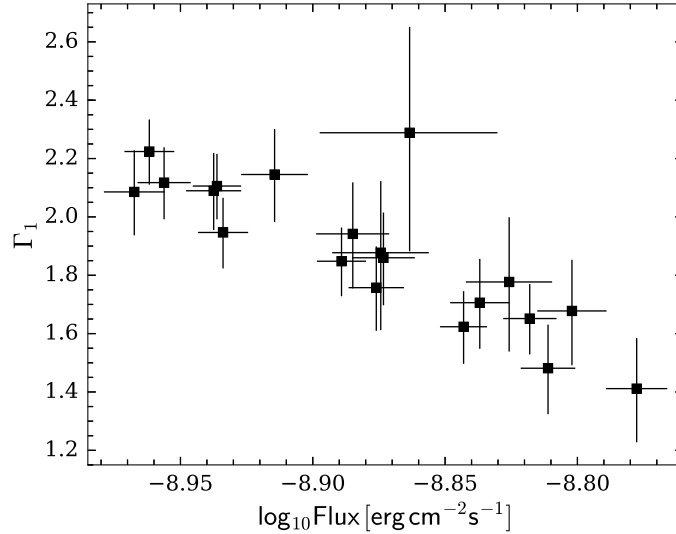


Figure 4. Variation of Γ_1 with Flux in the 0.7–30 keV band obtained from the time-resolved spectral analysis using the model *constant × TBabs(Synconv ⊗ bknpower)*.

During Oct 25–26, 2017 *Swift* has carried one observation for an exposure of 987 secs in two orbits in the Windowed timing (WT) mode. However, during the first orbit, the image is too near the edge of the WT window, which resulted in loss of photon counts, hence we skipped the first orbit in our analysis. We obtained the spectrum for the second orbit having an exposure of 499 sec using an online tool available at the UK *Swift* Science Data Centre (Evans et al. 2009). The second orbit falls in the 15th time-segment (corresponding time 70 ksec) of our time resolved spectral analysis. We carried out the simultaneous spectral fit of the *Swift*-XRT (0.7–7 keV), SXT (0.7–7 keV) and LAXPC (3–30 keV) spectra with the synchrotron convolved broken power law model. The model fitted the spectrum well with a reduced- χ^2 of 1.01, and the best fit parameters are obtained as $\Gamma_1 = 2.19^{+0.22}_{-0.24}$, $\Gamma_2 = 4.36^{+0.09}_{-0.09}$ and $n_{bkn} = 1.04^{+0.02}_{-0.02}$. The obtained spectral index, Γ_1 is consistent with that acquired in the time resolved spectral analysis (see Table 3).

3.3 Correlation between particle density and Index

The X-ray variability in flux and spectral parameters of 1ES 1959+650 observed by *AstroSat* can be used to obtain information about the physical parameters of the emission region. Theoretically, it is easier to obtain the predicted rela-

tion between index and the particle density at a given energy rather than between the index and the flux. Thus we also estimated the particle density variation.

The normalisation of the broken power-law model is such that it is equal to the particle density at the break energy, i.e. at $\xi_{brk} = \sqrt{C}\gamma_{brk}$, such that $E_{brk} = \xi_{brk}^2$. However this is a matter of choice and the model can be recasted such that the normalisation is equal to the density at any chosen particle energy ξ . For the time-averaged spectrum we computed the normalisation and its error for different values of ξ and found that for ξ^2 (or E) = 1.21 keV, the error on the normalisation i.e. the particle density at $\xi^2 = 1.21$ keV, is the smallest. Hence we took this value as the reference energy. Note that this energy is smaller than the break one and hence we look for correlation between the normalised particle density variation $\Delta n_\gamma(\xi_{ref}) / < n_\gamma(\xi_{ref}) >$ (where $< n_\gamma(\xi_{ref}) > = 1.20$) and the variation in lower energy index i.e. $\Delta\Gamma_1$ (i.e. deviation of Γ_1 from their means 1.88) as shown in Figure 5. An anti-correlation is seen (Spearman rank correlation ~ -0.68 with probability 0.001) which is not as strong as that between the flux and the index (Spearman rank correlation ~ -0.8 with probability 2.5×10^{-5}). This is perhaps expected since the definition of flux makes it a function of the normalisation of the particle density and index, and some of the observed anti-correlation can be at-

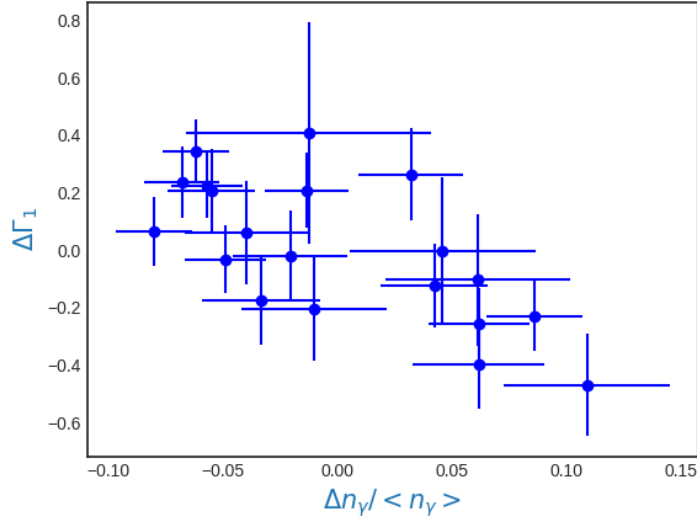


Figure 5. Plot between the variation of $\Delta\Gamma_1$ with the normalised particle density variation $\Delta n_\gamma(\xi_{ref})/\langle n_\gamma(\xi_{ref}) \rangle$ of the model $constant \times TBabs(Synconv \otimes bknpower)$ fitted to the time-resolved spectral bins.

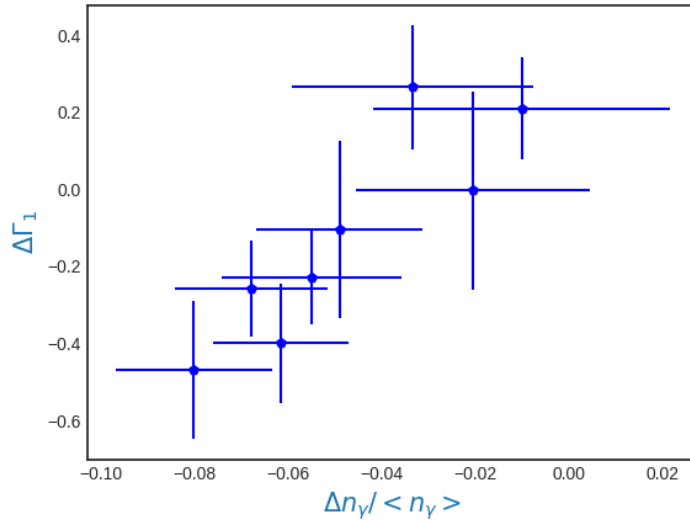


Figure 6. Plot between $\Delta\Gamma_1$ and $\Delta n_\gamma(\xi_{ref})/\langle n_\gamma(\xi_{ref}) \rangle$ when the Γ_1 is shifted by 60 ksec.

tributed to this dependence on index. It is interesting to note that a better correlation is obtained when the index is shifted by 60 ksecs (Figure 6), i.e. a time-lag is introduced between them (Spearman rank correlation ~ 0.9 with probability 0.002). In other words, a strong correlation is obtained between the low-energy index and particle density for segments which are 60 ksec apart. This can be qualitatively illustrated by plotting the normalised particle density variation $\Delta n_\gamma(\xi_{ref})/\langle n_\gamma(\xi_{ref}) \rangle$ and $\Delta\Gamma_1$ as a function of time as shown in Figure 7. While we discuss the implication of this behaviour in the next section, at this stage it is worth noting that the amplitude of the variation of particle density

$|\Delta n_\gamma(\xi_{ref})/\langle n_\gamma(\xi_{ref}) \rangle| \sim 0.1$ is significantly smaller than for the index $|\Delta\Gamma_1| \sim 0.5$.

4 MODELING THE SPECTRAL VARIABILITY

The X-ray emission of HBL sources is typically modelled as synchrotron emission, which is produced by a non-thermal electron distribution gyrating in an ambient magnetic field. The emission is most likely to be associated with a shock, which provides favourable conditions for the particles to get accelerated through the Fermi acceleration process. Keeping these features in mind, we investigated the predictions of

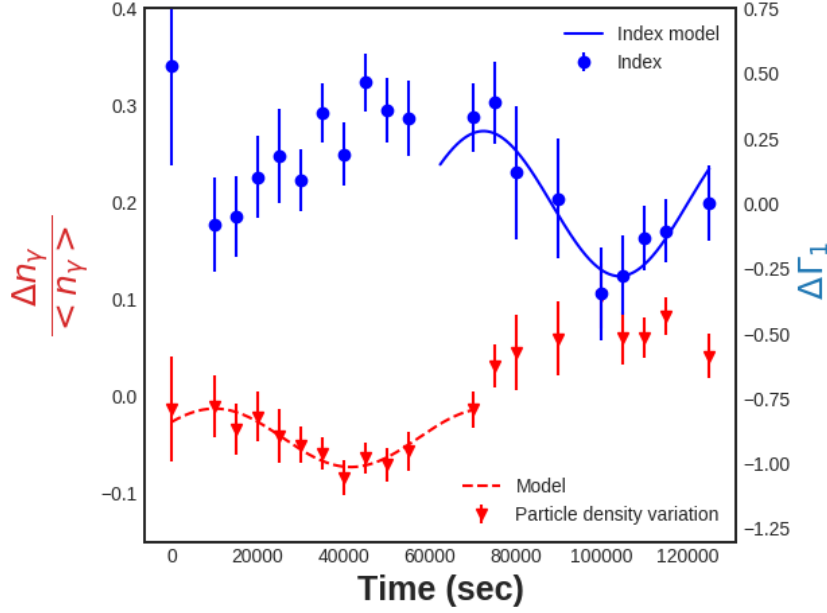


Figure 7. $\Delta n_\gamma / n_\gamma$ and $\Delta \Gamma_1$ light curves showing a time delay of nearly ~ 60 ks. The red dotted curve corresponds to input sinusoidal variation of $\frac{\Delta n_c}{n_c}$ (equation 13), while the blue solid curve is the corresponding index variation obtained using equation 14.

such a model for the variability on the index Γ_1 and its relation with that of the particle number density.

We assume that the observed emission arises from a relativistic spherical blob which is moving towards the line of sight of the observer with Doppler factor $\delta = \frac{1}{\Gamma(1-\beta \cos \theta)}$, where Γ is the bulk Lorentz factor of the blob and θ is the angle between the jet axis and line of sight of observer. The spherical blob includes an acceleration region (which includes a shock) where injected low energy electrons are continuously accelerated to high energies. The electrons escaping from the acceleration region enter into a cooling region, where they cool through synchrotron and Inverse Compton processes. We assume that the acceleration and the cooling region are spatially separated and that the escape rate from the acceleration region is equal to the injection rate in the cooling region. For such a model, the steady state particle distribution in the cooling region is a broken power-law as assumed in the spectral fitting in the previous section. For particles with energy greater than the break energy, radiative cooling is important while for lower energy ones cooling is insignificant. Since the motivation here is to predict the correlation between the normalisation and index below the break energy, we consider the case when radiative cooling is not important.

In the acceleration region, the time evolution of the particle distribution can be written in-terms of a partial differential equation as

$$\frac{\partial n_a}{\partial t} + \frac{\partial}{\partial \gamma} \left\{ \left[\left(\frac{d\gamma}{dt} \right)_{acc} - \left(\frac{d\gamma}{dt} \right)_{loss} \right] n_a \right\} + \frac{n_a}{\tau_{esc}} = 0, \quad (1)$$

where γ is Lorentz factor of electron, n_a is number density (in units of cm^{-3}) of the electrons in the acceleration region, first and second term in square bracket accounts for the acceleration rate and energy loss rates respectively, and $\frac{n_a}{\tau_{esc}}$

describes the escape from the acceleration region at rate τ_{esc}^{-1} . The acceleration term in the equation is approximated by

$$\left(\frac{d\gamma}{dt} \right)_{acc} = \frac{\gamma}{\tau_{acc}} \quad (2)$$

For synchrotron cooling, the energy-loss rate is given by

$$\left(\frac{d\gamma}{dt} \right)_{loss} = \beta_s \gamma^2 \quad (3)$$

where $\beta_s \sim \frac{1}{\gamma_{max} \tau_{acc}} = \frac{4}{3} \frac{\sigma_T B^2}{8\pi m_e c}$. Here B is the magnetic field in the acceleration region, σ_T is the Thomson cross section and m_e is the electron mass.

The accelerated particles finally escape into the cooling region, where they subsequently lose most of energy into radiation. Since, as mentioned above we are interested in the spectra below the break energy, we ignore the cooling term in this region and hence we solve the kinetic equation of particle distribution for $\gamma \lesssim \gamma_{brk}$. In such cases, the evolution of particle distribution in the cooling region can be described by the equation

$$\frac{\partial n_c}{\partial t} = \frac{n_c}{\tau_{esc,c}} + \frac{n_a}{\tau_{esc}} \quad (4)$$

Note that in this interpretation the observed synchrotron spectrum is produced by the non-thermal electrons in the cooling region given by $n_c(\gamma)$.

The steady state solution of equation 1 can be obtained as

$$n_a(\gamma) = K \gamma_0^{\frac{\tau_{acc}}{\tau_{esc}}} \left(1 - \frac{\gamma_0}{\gamma_{max}} \right)^{-\frac{\tau_{acc}}{\tau_{esc}}} \times \frac{1}{\gamma^2} \left(\frac{1}{\gamma} - \frac{1}{\gamma_{max}} \right)^{\frac{\tau_{acc}}{\tau_{esc}} - 1} \quad (5)$$

where K is constant and can be determined by boundary

Table 2. Best-fit parameters for the time-averaged spectra fitted with the synchrotron convolved *power-law*, logparabola (*logpar*) and broken-power-law (*bknpower*) models. The top panel corresponds to synchrotron convolved *power-law* model, Row:- 5: power law particle index, p ; and 6: normalisation, n_{pow} . Middle panel corresponds to synchrotron convolved *logpar* model, Row:- 5: α is the particle spectral index at the pivot energy ξ_{pivot}^2 ; 6: β is the curvature parameter; 7: ξ_{pivot} determines the pivot energy; and 8: normalisation, n_{logpar} . Bottom panel corresponds to synchrotron convolved *bknpower* model, Row:- 5: Γ_1 is the particle spectral index before the break energy; 6: Γ_2 is the particle spectral index after the break energy; 7: ξ_{brk} corresponds to the square root of break energy; and 8: normalisation, n_{bkn} . In each panel, Row 1 corresponds to hydrogen column density (N_H), and Row 2, 3, 4 corresponds to the model constant values for SXT, LAXPC 10, LAXPC 20 spectra, respectively;

Model Component	Parameters	χ^2/dof
power-law	N_H (10^{22}cm^{-2})	~ 0.2
	constant _{sxt}	1
	constant _{lax10}	~ 0.75
	constant _{lax20}	~ 0.82
	p	~ 3.5
	n_{pow}	~ 2.5
logpar	N_H (10^{22}cm^{-2})	0.04 ± 0.01
	constant _{sxt}	1
	constant _{lax10}	$0.73^{+0.01}_{-0.01}$
	constant _{lax20}	$0.84^{+0.02}_{-0.02}$
	α	$1.13^{+0.16}_{-0.18}$
	β	$2.35^{+0.18}_{-0.16}$
	ξ_{pivot} ($\sqrt{\text{keV}}$)	0.7
	n_{logpar} (10^{-2})	$2.87^{+0.22}_{-0.24}$
bknpower	N_H (10^{22}cm^{-2})	0.04 ± 0.02
	constant _{sxt}	1
	constant _{lax10}	$0.74^{+0.02}_{-0.02}$
	constant _{lax20}	$0.85^{+0.02}_{-0.02}$
	Γ_1	$1.83^{+0.27}_{-0.36}$
	Γ_2	$4.16^{+0.11}_{-0.09}$
	ξ_{brk} ($\sqrt{\text{keV}}$)	$1.69^{+0.14}_{-0.15}$
	n_{bkn}	1.29 ± 0.03

condition at some γ_0 or by introducing the mono-energetic injection $Q = Q_0\delta(\gamma - \gamma_0)$ in equation 1. In later case (mono-energetic injection), K is obtained as $Q_0\tau_{\text{acc}}$. Here we consider the case when the solution of equation 1 is determined by the boundary condition, while the alternate situation of a delta function injection is discussed in the end of this section. For $\gamma \ll \gamma_{\text{max}}$ and $\gamma_0 \ll \gamma_{\text{max}}$, the equation reduces to a power-law form,

$$n_a(\gamma) = \frac{K}{\gamma_0} \left(\frac{\gamma}{\gamma_0} \right)^{-\Gamma} \quad (6)$$

with $\Gamma = \frac{\tau_{\text{acc}}}{\tau_{\text{esc}}} + 1$ being the index. The corresponding steady state solution for the particle density in the cooling region becomes

$$n_c(\gamma) = \frac{K}{\gamma_0} \frac{\tau_{\text{esc},c}}{\tau_{\text{esc}}} \left(\frac{\gamma}{\gamma_0} \right)^{-\Gamma} \quad (7)$$

Now a variation in the acceleration time-scale $\Delta\tau_{\text{acc}}$ would lead to a variation in the index $\Delta\Gamma = \Delta\tau_{\text{acc}}/\tau_{\text{esc}}$. If the variation is a slow process such that it is significantly longer than the time-scales of the system, then the particle density would vary as

$$\frac{\Delta n_c(\gamma)}{n_c(\gamma)} = -\log\left(\frac{\gamma}{\gamma_0}\right) \Delta\Gamma \quad (8)$$

This implies that the density at some energy γ will be inversely correlated with the index as is observed. However, since γ is expected to be significantly larger than γ_0 , the amplitude of the density variation $|\Delta n_c(\gamma)/n_c(\gamma)| \gg |\Delta\Gamma|$, which is contrary to observations. Figure 7 shows that while $|\Delta n_c(\gamma)/n_c(\gamma)| \sim 0.1$, Γ shows a much larger variation with $\Delta\Gamma \sim 0.5$. Another way of expressing the problem, is that the power-law particle distribution pivots over γ_0 and since $\gamma \gg \gamma_0$, the density at γ should vary significantly for even small changes in index. However, the data shows that the magnitude of the variation of the density is smaller than that of the index. We note that the problem persists even when we consider the driving variability to be due to the escape time scale $\Delta\tau_{\text{esc}}$ or if we consider mono-energetic injection such that $K = Q_0\tau_{\text{acc}}$.

A possible solution maybe that the observed variability is not a slow variation and instead its time-scale is comparable to the time-scales of the systems such as the acceleration time-scale. In such cases, the steady state solutions are no longer valid and one has to solve the time dependent equations 1 and 4. We do this in the linear approximation and introduce a small sinusoidal perturbation in particle acceleration time scale

$$\tau_{\text{acc}}(t) = \tau_{\text{acc}} + \Delta\tau_{\text{acc}} e^{i\omega t} \quad (9)$$

which in the linear regime produce variation in the particle densities, $n_a(\gamma, t) = n_a(\gamma) + \Delta n_a e^{i\omega t}$ and $n_c(\gamma, t) = n_c(\gamma) + \Delta n_c e^{i\omega t}$. In such a case, the fractional change in particle density in the acceleration region for the sinusoidal perturbation in τ_{acc} is obtained as

$$\frac{\Delta n_a}{n_a(\gamma)} = \frac{\Delta\tau_{\text{acc}}}{i\omega\tau_{\text{acc}}\tau_{\text{esc}}} \left[\left(\frac{\gamma_0}{\gamma} \right)^{i\omega\tau_{\text{acc}}} - 1 \right] \quad (10)$$

and the corresponding variation in the cooling region for energies lower than the break energy, becomes

$$\frac{\Delta n_c}{n_c(\gamma)} = \frac{\Delta\tau_{\text{acc}}}{i\omega(1 - i\omega\tau_{\text{esc},c})(\tau_{\text{acc}}\tau_{\text{esc}})} \left[\left(\frac{\gamma_0}{\gamma} \right)^{i\omega\tau_{\text{acc}}} - 1 \right] \quad (11)$$

Now one can define a local particle density index as $\Gamma = -\left(\frac{\gamma}{n_c}\right) \frac{dn_c}{d\gamma}$ and its variation, $\Delta\Gamma$, can be written as

$$\begin{aligned} \Delta\Gamma &= -\gamma \frac{\partial}{\partial\gamma} \left(\frac{\Delta n_c}{n_c(\gamma)} \right) \\ &= \frac{\omega\tau_{\text{acc}}}{2} \frac{1}{\sin(\omega\tau_{\text{acc}} \log(\gamma_0/\gamma)/2)} \\ &\quad \times \exp(i\omega\tau_{\text{acc}} \log(\gamma_0/\gamma)/2) \frac{\Delta n_c}{n_c(\gamma)} \end{aligned} \quad (12)$$

At this stage, it is convenient to introduce a real sine function perturbation, instead of complex quantities and express the variation

$$\frac{\Delta n_c}{n_c} = N \sin(\omega t - \phi) \quad (13)$$

Table 3. Best fit parameters of time resolved spectral analysis fitted with the synchrotron convolved broken-power-law models. Col. 1: time bin in secs; 2: low energy particle spectral index; 3: high energy particle spectral index; 4: normalisation; 5: logarithm of Flux (erg cm⁻² s⁻¹); 6: χ^2 / degrees of freedom

Time	Γ_1	Γ_2	n_{bkn}	logF	χ^2/dof
0	$2.29^{+0.36}_{-0.41}$	$3.64^{+0.07}_{-0.07}$	$1.19^{+0.06}_{-0.07}$	$-8.86^{+0.03}_{-0.03}$	52.87 / 67
10000	$1.68^{+0.18}_{-0.19}$	$3.75^{+0.06}_{-0.06}$	$1.19^{+0.04}_{-0.04}$	$-8.8^{+0.01}_{-0.01}$	101.24 / 123
15000	$1.71^{+0.15}_{-0.16}$	$3.88^{+0.06}_{-0.06}$	$1.16^{+0.03}_{-0.03}$	$-8.84^{+0.01}_{-0.01}$	134.85 / 156
20000	$1.86^{+0.15}_{-0.16}$	$4.04^{+0.07}_{-0.07}$	$1.18^{+0.03}_{-0.03}$	$-8.87^{+0.01}_{-0.01}$	106.22 / 132
25000	$1.94^{+0.18}_{-0.19}$	$3.99^{+0.08}_{-0.07}$	$1.15^{+0.03}_{-0.03}$	$-8.88^{+0.01}_{-0.01}$	81.29 / 115
30000	$1.85^{+0.12}_{-0.12}$	$4.07^{+0.08}_{-0.08}$	$1.14^{+0.02}_{-0.02}$	$-8.89^{+0.01}_{-0.01}$	166.48 / 205
35000	$2.11^{+0.11}_{-0.11}$	$4.18^{+0.08}_{-0.08}$	$1.13^{+0.02}_{-0.02}$	$-8.94^{+0.01}_{-0.01}$	105.54 / 129
40000	$1.95^{+0.12}_{-0.12}$	$4.22^{+0.08}_{-0.08}$	$1.1^{+0.02}_{-0.02}$	$-8.93^{+0.01}_{-0.01}$	119.79 / 117
45000	$2.22^{+0.11}_{-0.11}$	$4.26^{+0.08}_{-0.08}$	$1.13^{+0.02}_{-0.02}$	$-8.96^{+0.01}_{-0.01}$	75.85 / 116
50000	$2.12^{+0.12}_{-0.13}$	$4.29^{+0.09}_{-0.09}$	$1.12^{+0.02}_{-0.02}$	$-8.96^{+0.01}_{-0.01}$	105.07 / 117
55000	$2.09^{+0.14}_{-0.15}$	$4.49^{+0.12}_{-0.11}$	$1.13^{+0.02}_{-0.02}$	$-8.97^{+0.01}_{-0.01}$	105.17 / 100
70000	$2.09^{+0.13}_{-0.13}$	$4.37^{+0.09}_{-0.09}$	$1.18^{+0.02}_{-0.02}$	$-8.94^{+0.01}_{-0.01}$	144.21 / 162
75000	$2.15^{+0.16}_{-0.16}$	$4.29^{+0.09}_{-0.09}$	$1.24^{+0.03}_{-0.03}$	$-8.91^{+0.01}_{-0.01}$	119.63 / 119
80000	$1.88^{+0.25}_{-0.27}$	$4.26^{+0.09}_{-0.09}$	$1.26^{+0.05}_{-0.05}$	$-8.87^{+0.02}_{-0.02}$	63.66 / 83
90000	$1.78^{+0.22}_{-0.24}$	$4.02^{+0.07}_{-0.07}$	$1.27^{+0.05}_{-0.05}$	$-8.83^{+0.02}_{-0.02}$	79.77 / 92
100000	$1.41^{+0.17}_{-0.18}$	$4.16^{+0.07}_{-0.07}$	$1.33^{+0.04}_{-0.05}$	$-8.78^{+0.01}_{-0.01}$	109.94 / 143
105000	$1.48^{+0.15}_{-0.16}$	$4.2^{+0.08}_{-0.07}$	$1.27^{+0.03}_{-0.04}$	$-8.81^{+0.01}_{-0.01}$	156.31 / 178
110000	$1.62^{+0.12}_{-0.13}$	$4.31^{+0.08}_{-0.08}$	$1.27^{+0.03}_{-0.03}$	$-8.84^{+0.01}_{-0.01}$	181.49 / 210
115000	$1.65^{+0.12}_{-0.12}$	$4.16^{+0.13}_{-0.12}$	$1.3^{+0.02}_{-0.03}$	$-8.82^{+0.01}_{-0.01}$	232.13 / 224
125000	$1.76^{+0.14}_{-0.15}$	$4.38^{+0.1}_{-0.09}$	$1.25^{+0.03}_{-0.03}$	$-8.88^{+0.01}_{-0.01}$	146.95 / 172

where N is some constant. The corresponding index variation can then be written as

$$\Delta\Gamma = -\frac{N}{\log(\gamma/\gamma_0)} \frac{\phi_{lag}}{\sin(\phi_{lag})} \sin(\omega t - \phi - \phi_{lag}) \quad (14)$$

where $\phi_{lag} = \omega\tau_{acc} \log(\gamma/\gamma_0)/2$ is the phase lag corresponding to a time delay $\tau_{lag} = \tau_{acc} \log(\gamma/\gamma_0)/2$ between the index and normalisation. It is evident that for slow variations, with ω tending to zero, $\phi_{lag}/\sin(\phi_{lag})$ tends to unity, and

the above equation reduces to equation derived from the steady state solution. Now, when the variation time-scale is comparable to the acceleration one, i.e. when ϕ_{lag} is not small, the term $\phi_{lag}/\sin(\phi_{lag})$ can be arbitrarily large. This means that the amplitude of $\Delta\Gamma$ can be much larger than that of $\frac{\Delta n_c}{n_c}$. However, in that case there will be a significant time-lag between the variation of the normalisation and the index. The equations have been derived in the rest frame

of the emitting region. In the observer's frame the change in the frequency would be $\omega_o = \omega\delta/(1+z)$, where z is the redshift and δ is Doppler factor.

We now check, if the observed variation of particle density and the index can be understood in this framework. The values of N , ω_o and ϕ are chosen such that equation 13 produces the shape of the particle density light curve as shown in Figure (7), where the red dashed curve is the input sinusoidal variation (equation 13) for $N = 3 \times 10^{-2}$, $\omega_o = 9.94 \times 10^{-5}$ and $\phi = 5.71$. The blue solid curve is the corresponding index variation obtained by using equation (14) with $\phi_{lag} = 6.21$ and $\log \gamma/\gamma_0 = 9.05$ after the expected time-delay of $\tau_{lag,o} = \phi_{lag}/\omega_o \sim 6.24 \times 10^4$ seconds. This further validates the correlation seen between the density and index after taking into account a time-lag shift as shown in Figure 6. Note that in the emission rest frame, $\tau_{lag} = \phi_{lag}/\omega \sim 6.24 \times 10^4 \delta/(1+z)$ secs and the corresponding $\tau_{acc} = 1.38 \times 10^4 \delta/(1+z)$ secs.

One can undertake a similar analysis for the case of when instead of having a fixed low energy boundary condition for the particle density, there is a mono-energetic injection of particles i.e. $Q = Q_0\delta(\gamma - \gamma_0)$ in equation 1, leading to $C = Q_0\tau_{acc}$. The analysis can also be done for the situation where the variability is driven by variation in the escape time-scale instead of the acceleration one. For both these cases, the variation of index $\Delta\Gamma$ turns out to be always significantly smaller than that of the density for any oscillation frequency. Thus, the observed large variation of Γ as compared to the density is compatible only with a model with acceleration time scale variability and a fixed low energy boundary condition for the particles.

We note and emphasize again in the next section, that the variability observed is only for a single cycle and hence the time delay inferred between the density and index can not be asserted with statistical significance. The point here is that the observed magnitudes of the density and index can be explained if the time-scale of variation is of the same order as the acceleration time-scale and the expected time-lag between them is consistent with the data.

5 SUMMARY & DISCUSSION

We have analysed the X-ray variability of 1ES 1959+650 observed during 26 October, 2017 by *AstroSat* for a total duration of ~ 135 ks. We found that the synchrotron convolved broken power-law model provided a better fit to the time averaged spectrum in the energy range 0.7–30 keV than the synchrotron convolved power-law and logparabola models (see Table 2). In order to examine the spectral and flux properties over finer time bins, we used the method of time-resolved spectroscopy, where the total observation period (~ 135 ks) was divided into time segments of 5 ksec. In each time bin, we found that the broken power-law model for the particle distribution yielded a good fit statistic (see Table 3). The SXT, LAXPC, UVIT-NUV and UVIT-FUV emission as measured by the *AstroSat* instrument shows evidence for variability. In this work we mainly concentrated on interpreting the correlations between X-ray spectral parameters obtained from the time-resolved analysis.

The lower energy particle index Γ_1 shows a marked anti-correlation with the 0.7–30 keV flux, the anti-correlation at

X-ray energies between the photon index and flux as has been observed in other sources (e.g. Gliozzi et al. 2006; Hayashida et al. 2015; Kapanadze et al. 2017). However, since it is more straightforward to interpret a correlation between the particle number density at a given energy with its index, we estimate the number density using the normalisation of the fit. The normalisation parameter can be chosen to correspond to the number density at different reference energies. We found it optimal to choose an energy reference E_{ref} (or ξ_{ref}^2) = 1.21 keV which is smaller than the typical measured break energy of E_{brk} (or ξ_{brk}^2) = 2.86 keV, since the errors on estimated number density was least for such a reference energy. The particle index Γ_1 was again found to anti-correlate with the number density, but with a lower significance as compared to its correlation with flux. The normalised variation of the particle density $\delta n_\gamma/n_\gamma$ was found to be ~ 0.1 which is less than the observed variation in index $\Delta\Gamma \sim 0.5$. Moreover, if the index variation was shifted by ~ 60 ksec, a correlation was seen between the index and number density, instead of the anti-correlation seen when such a shift was not introduced.

We model the system as having an acceleration region where a power-law energy distribution of electrons is created and escape to a cooling region. In the cooling region, their distribution takes the form of a broken power-law with radiative cooling important for particles with energy greater than the break energy and not important for lower energies. We argue that any variability on time-scale longer than the time-scales of the system, would lead to a normalised variation of the particle density at a reference energy, $\gamma_{ref} < \gamma_{brk}$ to be much larger than that of the index, $\Delta n_\gamma(\gamma_{ref})/n_\gamma(\gamma_{ref}) \gg \Delta\Gamma_1$, which is contrary to the observations. On the other hand, if there is variability in the acceleration time-scale τ_{acc} and this variability itself has a time-scale of the same order as the acceleration one, then the observed amplitudes of $\Delta n_\gamma(\gamma_{ref})/n_\gamma(\gamma_{ref})$ and $\Delta\Gamma_1$ can be explained. Moreover, such a model would predict a time-lag between the two and the data indeed shows that a near sinusoidal variation in the particle density is followed by a similar variation in index after a time-lag. This identification allows us to constrain physical parameters of the system such as the acceleration time scale $\tau_{acc} \sim 1.38 \times 10^4 \delta/(1+z)$ secs which for a Lorentz boosting factor $\delta \sim 15$ (Patel et al. 2018), turns out to be 1.97×10^5 secs. Then the escape time-scale can be estimated to be $\sim \tau_{acc}/(\Gamma_1 - 1) \sim 2.24 \times 10^5$ secs. If we assume that this corresponds to the R/c , then the size of the system turns out to be $R \sim 6.73 \times 10^{15}$ cms.

There are possible physical situations where the variation time-scale of the particle acceleration time-scale may be comparable to itself. A simplistic example would be where the acceleration time-scale for shock acceleration is expressed as nR_s/c , where R_s is the width of the shock and n is the average number of times an electron has to cross the shock to gain substantial energy. Now if a variability is introduced due to the variation of the shock width, the time-scale of the variability would be $R_s/|\dot{R}_s|$, where $|\dot{R}_s|$ is the magnitude of the rate of change of the width. This variability time-scale would be of the same order as the acceleration one if $\dot{R}_s \sim c/n$.

We reemphasise that the observed time-lag ~ 60 ksecs is of the order of the length of the observation and the inference is based only one oscillation cycle. What is required

is significantly longer duration of observation (say 10 times the observation time used in the present work) to statistically confirm the time-lag. Even for such an observation, complexities would arise if the magnetic field or the Doppler factor varies during the observation which would mean that the reference energy at which the particle density is being measured would not correspond to the same particle energy. It should also be noted that the broken power-law distribution used to fit the time-resolved spectra is at best an approximation to the real smooth distribution coming from a cooling region. The situation may be more complicated, if the micro-physics of the system is different, such as the escape or acceleration time-scale being dependent on the energy of the particle. Spectral curvature observed in several sources indicate that this indeed be the case (Massaro et al. 2004; Jagan et al. 2018; Goswami et al. 2018, 2020b,a). In fact X-ray spectral modelling of 1ES 1959+650 spectra during the period 2015 August – 2017 November (when it was in a high flux state) required a log-parabola model with a wide range of curvature values (e.g. Kapanadze et al. (2016b,a, 2018b,a); Patel et al. (2018); Wang et al. (2019)). This source also shows wide variation for the peak energy which ranges from ~ 0.1 to ~ 7.7 keV (Kapanadze et al. 2018a). In summary, although the intrinsic spectral behaviour of blazars is expected to be complex, the relative amplitude of the particle density and index variations and the time-lag between them, can be effectively used to constrain the underlying physics.

6 ACKNOWLEDGEMENTS

This publication has made use of data from the *As-trosat* mission of the Indian Space Research Organisation (ISRO), archived at the Indian Space Science Data Centre (ISSDC). This work has used the data from the Soft X-ray Telescope (SXT) developed at TIFR, Mumbai, and the SXT POC at TIFR is thanked for verifying and releasing the data via the ISSDC data archive and providing the necessary software tools. LaxpcSoft software is used for analysis of the LAXPC data and we acknowledge the LAXPC Payload Operation Center (TIFR, Mumbai). We thank the UVIT POC at IIA, Bangalore for their support. This research has made use of data, software and/or web tools obtained from the High Energy Astrophysics Science Archive Research Center (HEASARC), a service of the Astrophysics Science Division at NASA/GSFC and of the Smithsonian Astrophysical Observatory's High Energy Astrophysics Division.

7 DATA AVAILABILITY

The data and the model used in this article will be shared on reasonable request to the corresponding author, Zahir Shah (email: zahir@iucaa.in) or Savithri H. Ezhikode (email: savithri@iucaa.in).

REFERENCES

Abdo A. A., et al., 2010, *ApJ*, **716**, 30
Agrawal P. C., 2017, *Journal of Astrophysics and Astronomy*, **38**, 27

Agrawal P. C., et al., 2017, *Journal of Astrophysics and Astronomy*, **38**, 30
Aliu E., et al., 2014, *ApJ*, **797**, 89
Antia H. M., et al., 2017, *ApJS*, **231**, 10
Błażejowski M., Sikora M., Moderski R., Madejski G. M., 2000, *ApJ*, **545**, 107
Böttcher M., 2005, *ApJ*, **621**, 176
Böttcher M., et al., 2003, *ApJ*, **596**, 847
Bregman J. N., Lebofsky M. J., Aller M. F., Rieke G. H., Aller H. D., Hodge P. E., Glassgold A. E., Huggins P. J., 1981, *Nature*, **293**, 714
Dermer C. D., Schlickeiser R., Mastichiadis A., 1992, *A&A*, **256**, L27
Elvis M., Plummer D., Schachter J., Fabbiano G., 1992, *ApJS*, **80**, 257
Evans P. A., et al., 2009, *MNRAS*, **397**, 1177
Gaur H., 2014, *Journal of Astrophysics and Astronomy*, **35**, 241
Ghisellini G., Padovani P., Celotti A., Maraschi L., 1993, *ApJ*, **407**, 65
Giebels B., et al., 2002, *ApJ*, **571**, 763
Gliozzi M., Sambruna R. M., Jung I., Krawczynski H., Horan D., Tavecchio F., 2006, *ApJ*, **646**, 61
Goswami P., Sahayanathan S., Sinha A., Misra R., Gogoi R., 2018, *MNRAS*, **480**, 2046
Goswami P., Sahayanathan S., Sinha A., Gogoi R., 2020a, *MNRAS*,
Goswami P., et al., 2020b, *MNRAS*, **492**, 796
Graff P. B., Georganopoulos M., Perlman E. S., Kazanas D., 2008, *ApJ*, **689**, 68
Gregory P. C., Condon J. J., 1991, *ApJS*, **75**, 1011
Gutierrez K., et al., 2006, *ApJ*, **644**, 742
Hayashida M., et al., 2015, *ApJ*, **807**, 79
Holder J., et al., 2003, *ApJ*, **583**, L9
Hovatta T., et al., 2014, *MNRAS*, **439**, 690
Jagan S. K., Sahayanathan S., Misra R., Ravikumar C. D., Jeena K., 2018, *MNRAS*, **478**, L105
Jones T. W., O'dell S. L., Stein W. A., 1974, *ApJ*, **188**, 353
Joseph P., Stalin C. S., Tandon S. N., Ghosh S. K., 2021, Curvit: An open-source Python package to generate light curves from UVIT data ([arXiv:2101.06377](https://arxiv.org/abs/2101.06377))
Kalberla P. M. W., Burton W. B., Hartmann D., Arnal E. M., Bajaja E., Morras R., Pöppel W. G. L., 2005, *A&A*, **440**, 775
Kapanadze B., 2017, The Astronomer's Telegram, **10743**, 1
Kapanadze B., Romano P., Vercellone S., Kapanadze S., Mdzinarishvili T., Kharshiladze G., 2016a, *MNRAS*, **457**, 704
Kapanadze B., Dorner D., Vercellone S., Romano P., Kapanadze S., Mdzinarishvili T., 2016b, *MNRAS*, **461**, L26
Kapanadze B., Dorner D., Romano P., Vercellone S., Kapanadze S., Tabagari L., 2017, *ApJ*, **848**, 103
Kapanadze B., et al., 2018a, *ApJS*, **238**, 13
Kapanadze B., et al., 2018b, *MNRAS*, **473**, 2542
Kirk J. G., Mastichiadis A., 1999, *Astroparticle Physics*, **11**, 45
Krawczynski H., et al., 2004, *ApJ*, **601**, 151
MAGIC Collaboration et al., 2020, *A&A*, **638**, A14
Mannheim K., Biermann P. L., 1992, *A&A*, **253**, L21
Maraschi L., Ghisellini G., Celotti A., 1992, *ApJ*, **397**, L5
Massaro E., Perri M., Giommi P., Nesci R., 2004, *A&A*, **413**, 489
Mastichiadis A., Kirk J. G., 1997, *A&A*, **320**, 19
Misra R., et al., 2017, *ApJ*, **835**, 195
Mücke A., Protheroe R. J., 2001, *Astroparticle Physics*, **15**, 121
Nishiyama T., 1999, in 26th International Cosmic Ray Conference (ICRC26), Volume 3. p. 370
Patel S. R., Shukla A., Chitnis V. R., Dorner D., Mannheim K., Acharya B. S., Nagare B. J., 2018, *A&A*, **611**, A44
Perlman E. S., et al., 1996, *ApJS*, **104**, 251
Rao A. R., Bhattacharya D., Bhalarao V. B., Vadawale S. V., Sreekumar S., 2017, arXiv e-prints, p. [arXiv:1710.10773](https://arxiv.org/abs/1710.10773)
Rybicki G., Lightman A., 2008, Radiative Processes in Astro-

- physics. Physics textbook, Wiley, <https://books.google.co.in/books?id=eswe2StAspsC>
- Shah Z., Sahayanathan S., Mankuzhiyil N., Kushwaha P., Misra R., Iqbal N., 2017, *MNRAS*, **470**, 3283
- Sikora M., Begelman M. C., Rees M. J., 1994, *ApJ*, **421**, 153
- Singh K. P., et al., 2016, In-orbit performance of SXT aboard AstroSat. p. 99051E, [doi:10.1117/12.2235309](https://doi.org/10.1117/12.2235309)
- Singh K. P., et al., 2017, *Journal of Astrophysics and Astronomy*, **38**, 29
- Tandon S. N., et al., 2017a, *Journal of Astrophysics and Astronomy*, **38**, 28
- Tandon S. N., et al., 2017b, *AJ*, **154**, 128
- Ulrich M.-H., Maraschi L., Urry C. M., 1997, *ARA&A*, **35**, 445
- Urry C. M., Padovani P., 1995, *PASP*, **107**, 803
- Wang Y., Zhu S., Xue Y., Gu M., Weng S., Le H. A. N., 2019, *ApJ*, **885**, 8
- Yadav J. S., et al., 2016a, *ApJ*, **833**, 27
- Yadav J. S., et al., 2016b, Large Area X-ray Proportional Counter (LAXPC) instrument onboard ASTROSAT. p. 99051D, [doi:10.1117/12.2231857](https://doi.org/10.1117/12.2231857)

This paper has been typeset from a $\text{\TeX}/\text{\LaTeX}$ file prepared by the author.